

Mesoscale to Submesoscale Transition in the California Current System. Part I: Flow Structure, Eddy Flux, and Observational Tests

X. CAPET, J. C. MCWILLIAMS, M. J. MOLEMAKER, AND A. F. SHCHEPETKIN

Institute of Geophysics and Planetary Physics, University of California, Los Angeles, Los Angeles, California

(Manuscript received 2 August 2006, in final form 13 April 2007)

ABSTRACT

In computational simulations of an idealized subtropical eastern boundary upwelling current system, similar to the California Current, a submesoscale transition occurs in the eddy variability as the horizontal grid scale is reduced to $O(1)$ km. This first paper (in a series of three) describes the transition in terms of the emergent flow structure and the associated time-averaged eddy fluxes. In addition to the mesoscale eddies that arise from a primary instability of the alongshore, wind-driven currents, significant energy is transferred into submesoscale fronts and vortices in the upper ocean. The submesoscale arises through surface frontogenesis growing off upwelled cold filaments that are pulled offshore and strained in between the mesoscale eddy centers. In turn, some submesoscale fronts become unstable and develop submesoscale meanders and fragment into roll-up vortices. Associated with this phenomenon are a large vertical vorticity and Rossby number, a large vertical velocity, relatively flat horizontal spectra (contrary to the prevailing view of mesoscale dynamics), a large vertical buoyancy flux acting to restratify the upper ocean, a submesoscale energy conversion from potential to kinetic, a significant spatial and temporal intermittency in the upper ocean, and material exchanges between the surface boundary layer and pycnocline. Comparison with available observations indicates that submesoscale fronts and instabilities occur widely in the upper ocean, with characteristics similar to the simulations.

1. Introduction

Wind-driven currents exhibit mesoscale instabilities, and the resulting mesoscale eddies are typically the flow type with the largest kinetic energy in the ocean (besides the tides). The prevailing dynamical paradigm for the general circulation encompasses these large- and mesoscale currents together with mixing and dissipation primarily caused by microscale flows (e.g., turbulent boundary layers and breaking internal waves). In this paper and its companions (Capet et al. 2008, hereinafter Part II; 2006, manuscript submitted to *J. Phys. Oceanogr.*, hereinafter Part III), we investigate the existence and dynamical importance of submesoscale currents at an intermediate scale, as another potentially important element of the oceanic general circulation.

As yet relatively little is known about submesoscale currents because of limitations in instrumental sam-

pling and computational resolution. We provisionally define the submesoscale regime as a spatial scale just smaller than the mesoscale: a horizontal scale of $O(10)$ km, less than the first baroclinic deformation radius; a vertical scale of $O(10)$ m, thinner than the main pycnocline; and a time scale of $O(1)$ day, comparable to a lateral advection time for submesoscale feature by a mesoscale velocity. Our conceptual model for submesoscale currents, to be tested in this paper, is as follows: 1) they arise dynamically through advective interactions with mesoscale currents (and thus are distinct from inertia-gravity waves on comparable spatial scales); 2) they are importantly influenced by the earth's rotation and stratification (unlike many microscale flows); and 3) they are surprisingly energetic from the perspective of quasigeostrophic turbulence theory (Charney 1971) that is widely considered applicable to mesoscale currents [viz., the eddy energy has an "inverse" cascade toward larger scales and, hence, is depleted at small scales, and the Rossby $[V/(fL)]$ and Froude $[V/(NH)]$ numbers do not increase as the scale decreases; so the assumptions of quasigeostrophy are dynamically consistent down to arbitrarily small scales

Corresponding author address: Xavier Capet, IGPP/UCLA, 405 Charles E. Young Dr., Los Angeles, CA 90095-1567.
E-mail: capet@atmos.ucla.edu

(V is a velocity, f is a Coriolis frequency, N is the stratification frequency, and H and L are vertical and horizontal length scales)).

We make our investigation of submesoscale currents in the context of a subtropical, eastern boundary, upwelling regime (e.g., the California Current system; Marchesiello et al. 2003). Equatorward winds drive offshore Ekman transport, coastal upwelling, and along-shore currents with strong vertical shear. Surface heating supports strong stratification in the upper ocean except in the cold upwelling zone. Energetic mesoscale eddies develop from primarily baroclinic instability of the alongshore currents and are important in contributing to the mean circulation by cross-shore heat flux and depletion of mean available potential energy. There are observational indications that this regime has substantial submesoscale variability associated with the intense interweaving between warm offshore water and cold recently upwelled water (Brink and Cowles 1991). Particular features are cold temperature filaments (Paduan and Niiler 1990), surface temperature fronts that spawn submesoscale vortices (Flament et al. 1985), and surface spiral vortices (DiGiacomo and Holt 2001). Elsewhere there is ample evidence of both surface density fronts with at least a submesoscale width (Voorhis and Bruce 1982; Pollard and Regier 1992; Rudnick 1996) and long-lived submesoscale, subsurface vortices (McWilliams 1985), suggesting that submesoscale variability is widespread if not nearly ubiquitous.

In considering submesoscale dynamics, there are several important open issues. One issue is their generation mechanism. Frontogenesis is well known in the atmosphere as an evolutionary stage in storms growing out of the instability of the westerly winds, with increasingly thin fronts developing in regions of high strain rate on the edge of synoptic-scale circulations (Hoskins and Bretherton 1972; Hoskins and West 1979); in the ocean, by analogy, we might expect submesoscale fronts to spontaneously emerge during the evolution of mesoscale eddies. Alternatively, short-wavelength, secondary instabilities can develop, for example, from the mesoscale eddies directly or from the frontal flows themselves (McCreary et al. 1991; Barth 1994; Durski and Allen 2005; Boccaletti et al. 2007; Mahadevan and Tandon 2006). Since the strongest fronts occur at the surface, another issue is their role in material exchanges between the surface boundary layer and the interior pycnocline, whether as part of an advective subduction process aided by the relatively large vertical velocities near fronts or by the process of wind-induced buoyancy flux (Thomas and Lee 2005; Thomas 2005); if so, how deeply does the submesoscale flux penetrate? Yet another issue is whether submesoscale currents induce

significant forward cascades of kinetic energy and tracer variance down to dissipation at the microscales (i.e., opposite to the inverse energy cascade in quasi-geostrophic turbulence) and whether, in doing so, they break the constraints of hydrostatic, geostrophic, or gradient-wind force balances (i.e., the velocity is “unbalanced”) that accurately characterize most large- and mesoscale flows (McWilliams 2003; Molemaker et al. 2005). If unbalanced flows do spontaneously develop, this strengthens the plausibility of an important downscale route to dissipation in the oceanic interior for the general circulation through its associated mesoscale turbulence (McWilliams et al. 2001; Müller et al. 2005).

The basis for our investigation is a set of idealized, statistical equilibrium, upwelling simulations that differ from each other only by their horizontal resolution. We will show that this set spans a behavioral transition from a mean eastern boundary circulation with wholly mesoscale variability to the emergence of additional vigorous submesoscale variability. By going to resolutions as high as 750 m—well beyond what is required to simulate mesoscale phenomena (Marchesiello et al. 2003)—and comparing with coarser resolutions where submesoscale activity is suppressed, we are able to assess the structure of the emergent submesoscale circulation and to address the dynamical issues listed in the preceding paragraph. In this first paper we focus on the structure of submesoscale currents and material fields (tracers) and on their time-averaged eddy fluxes in the maintenance of the mean boundary current system. Dynamical analyses relevant to the submesoscale transition are presented in Part II, and the energy balance and flux across scales are analyzed in Part III.

2. Problem setup

The Regional Oceanic Modeling System (ROMS; Shchepetkin and McWilliams 2005, 2006) is configured to simulate an idealized version of the California Current system under a sustained wind field typical of the summer season and favoring coastal upwelling. The domain [hereinafter idealized California Current (ICC)] has a $720 \text{ km} \times 720 \text{ km}$ horizontal extent. The coastline is straight, and the ocean depth is uniformly set to 3500 m (flat bottom). There are 40 grid levels in the vertical with 15 levels above 50-m depth, yielding higher resolution near the surface. Comprehensive Ocean–Atmosphere Dataset (COADS) climatological fields for July (Da Silva et al. 1994) provide an atmospheric forcing (momentum, freshwater, and heat) that is both smooth in space and constant in time. Heat and freshwater fluxes are also adjusted with a restoring term to prevent the model surface fields from drifting away from climatological values (Barnier et al. 1995). Vertical mixing of

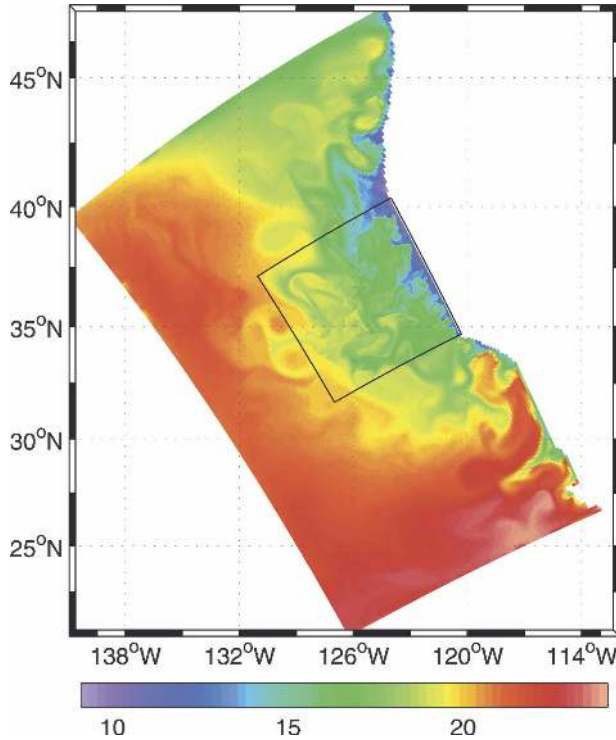


FIG. 1. Instantaneous SST at $t = 30$ days. The SST computed from ICC3 is superimposed onto the full USW12 field. The boundaries of the ICC domains are delineated by black lines.

tracers and momentum is done with a k -profile parameterization (KPP; Large et al. 1994). ROMS uses the full equation of state for seawater, and we will do the dynamical analyses in terms of potential temperature T and potential density ρ (with a surface reference level) to remove compressibility effects.

Five ICC cases are run (ICC12, ICC6, ICC3, ICC1, and ICC0) that differ in their horizontal gridpoint spacings: 12, 6, 3, 1.5, and 0.75 km. Open-ocean boundary conditions are obtained from a larger-scale (2200 km latitude \times 1500 km longitude) ROMS configuration with 12-km horizontal grid spacing (USW12) using climatological data and adaptive boundary conditions at the open-ocean boundaries (Marchesiello et al. 2001). USW12 generously encompasses the ICC domain (Fig. 1). It is run with topography, coastline, and surface forcing consistent with those within the ICC domain. USW12 sea level η , potential temperature T , salinity S , and horizontal velocity (u cross-shore and v along-shore) fields are saved with 5-day averages for the ICC adaptive lateral boundary conditions. A mild sponge layer along the open-ocean boundary of the ICC domain, with a horizontal viscosity varying linearly from 30 to 0 $\text{m}^2 \text{s}^{-1}$ over 72 km, helps to suppress potential inconsistencies between ICC and USW12 dynamics. The assumption underlying this approach is that sub-

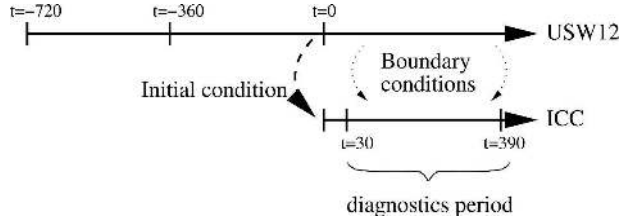


FIG. 2. Spinup procedure for the USW12 and ICC solutions (defined in text). Times are in days.

mesoscale activity developing at higher resolutions does not have significant upscaling effects on the mesoscale or mean circulation outside the ICC domain. Provided this is true, the offline nesting procedure ensures that boundary conditions applied on the edges of ICC are reasonably compatible with its mean and mesoscale interior dynamics. It is noteworthy that the energy sources for large-scale and mesoscale currents—subtropical-gyre winds and California Current System instabilities, respectively—differ from the ones at the submesoscale. While the latter can only be generated locally and strongly depend on the ICC resolution, the former are both passed through the lateral boundary conditions and modulated by the interior dynamics within the ICC. Because of its smoothness, the wind is not a significant source of energy except for the mean flow.

All of the ICC runs are initialized by interpolating the USW12 η , T , S , u , and v fields after 2 yr of simulation. An increase of turbulent eddy variability quickly develops within the higher-resolution ICC solutions, especially near the surface. Roughly 30 days after ICC initialization, the surface horizontal kinetic energy approaches a maximum and starts exhibiting fluctuations. We consider the spinup to be completed at this time. The solutions are computed for an additional 360 days, during which all physical variables are stored once per day, as both instantaneous fields and daily averages. This initialization procedure is summarized in Fig. 2. Statistical diagnostics are performed over the final 360 days, unless stated otherwise. In particular, the mean for any given quantity is defined as the average over this period.

3. Mean circulation

The mean circulation and thermohaline structure (Fig. 3) fit into the general picture of a subtropical eastern boundary system at the peak of the upwelling season. The offshore Ekman transport in $u < 0$ is confined within a surface layer that is 20–30 m thick. Deeper, a broad, slow, shoreward return flow is present, geostrophically supported by an equatorward alongshore pressure gradient (not shown). This return flow in $u >$

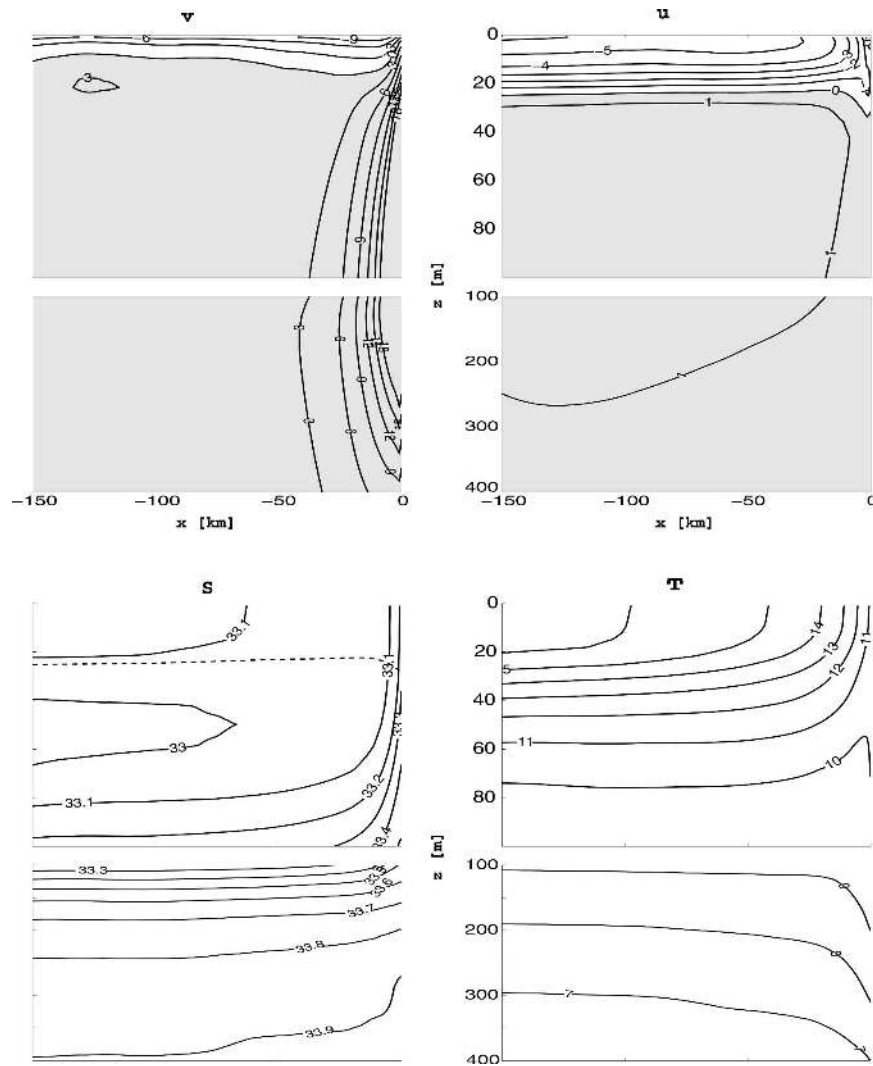


FIG. 3. Mean circulation: cross-shore sections of time- and alongshore-averaged u and v (cm s^{-1}), S (ppt), and T ($^{\circ}\text{C}$) for case ICC0. (All ICC cases are similar in these quantities.) The averaged boundary layer depth (as diagnosed by KPP) is drawn as the dashed line in the S panel.

0 partly feeds the coastal upwelling ($w > 0$; not shown), and it partly turns poleward as an undercurrent in $v > 0$. There is also significant vertical shear upward to the equatorward surface current $v < 0$ in thermal wind balance with the cross-shore η and pycnocline T gradients. The coastal upwelling is confined into an increasingly narrow layer of two to three grid points¹ where velocities increase with resolution up to 50 m day^{-1} in ICC0 (not shown); however, the integrated upward transport

¹ The singular width for coastal upwelling in idealized settings has been noted before (Pedlosky 1978). It disappears with shoaling topography (Mitchum and Clarke 1986).

is invariant with resolution. This means that the primary source of kinetic energy for the system, the mesoscale instability of the mean $v(x, z)$, is the same at all resolutions. (Because of this near-singular behavior in nearshore upwelling, we focus our analyses in the offshore region, excluding the nearshore within 80 km of the coast and sponge zones.) As typically found in the California Current System, the halocline is deeper than the thermocline and significantly below the boundary layer base. Although there is no topographic variation in the ICC domain, the solutions exhibit weak time-averaged standing eddies in accord with ones present in USW12 (where capes are present outside the ICC domain).

4. Velocity and tracer structure

The effect of horizontal resolution on instantaneous patterns for T and ρ (potential density) is shown in Fig. 4. After only $t = 30$ days after initialization, the phase coherence among the ICC solutions is still high, and the dominant mesoscale patterns can be recognized across all solutions. However, additional structural complexity emerges at smaller scales permitted by increases in the grid resolution. Most notably, $T(x, y)$ in ICC0 exhibits intense submesoscale activity within the surface boundary layer ($z = -10$ m). The temperature gradients are extremely strong and are indicative of efficient submesoscale frontogenesis (section 2 of Part II). Submesoscale wiggles are prevalent, especially in the regions with large temperature gradient, that is, at the edges of the mesoscale eddies. The concentration of submesoscale activity between the eddies and the exclusion in the eddy centers are strikingly evident in vertical vorticity, $\zeta^z = \partial_x v - \partial_y u$, and accompanying η (Fig. 5). The submesoscale vorticity structures are characterized by $O(1)$ Rossby numbers (i.e., $|\zeta^z| \gtrsim f$) that occur principally on the periphery of the mesoscale eddies, where their strain rate is high [i.e., $(\partial_x u - \partial_y v)^2 + (\partial_x v + \partial_y u)^2 \gtrsim f^2$; not shown]. In contrast, $|\zeta^z|$ is much smaller in the center of the mesoscale eddies, where the submesoscale structures are sparser and the mesoscale strain rate is smaller. Because of large Rossby numbers, we expect the submesoscale flows to be significantly ageostrophic (although submesoscale activity does imprint on sea level in Fig. 5), and this is assessed in section 5 of Part II. In the same regions where $|\zeta^z|$ is large, the vertical velocity w is also large (section 7 herein).

The enhancement in submesoscale velocity fluctuations required to produce submesoscale wiggles in tracers (Bartello 2000) is confirmed by velocity and tracer spectra (Fig. 6).² Overall, the spectra have shallower slopes at high wavenumbers as the horizontal resolution increases—especially for $k \gtrsim 5 \times 10^{-5} \text{ rad m}^{-1}$, corresponding to a radian scale of $L = k^{-1} \lesssim 20 \text{ km}$ —while of course also extending their wavenumber range to larger k . However, the magnitude of the spectrum shape change differs with quantity and depth. For surface velocity at the highest resolutions (ICC0 and ICC1), the spectrum slopes are close to -2 over 1.5 decades in k , noticeably shallower than the -3 value for the enstrophy inertial range in quasigeostrophic turbulence (Charney 1971). This indicates a significant de-

gree of (kinetic) energization in the submesoscale regime. In contrast, the subsurface velocity spectrum undergoes a less dramatic change, and the spectrum slopes remain steeper than -3 , albeit increasing modestly with resolution. Thus, the submesoscale transition is much more dramatic near the surface. Note the relatively small changes in the velocity spectra near their peak wavenumber in the mesoscale, $k \approx 2 \times 10^{-5} \text{ rad m}^{-1}$ ($L \approx 50 \text{ km}$), during the submesoscale transition. This result may be due to the strong mesoscale constraint exerted on the ICC cases by their common lateral boundary conditions. In the intermediate range $2 \times 10^{-5} \lesssim k \lesssim 5 \times 10^{-5} \text{ rad m}^{-1}$, a small amount of kinetic energy increase occurs. This could be consistent with the existence of a kinetic-energy inertial range encompassing these wavenumbers, but we rule out such inertial range in Part III. Our interpretation is that submesoscale features project onto a wide wavenumber spectrum, both taken individually [e.g., as the spectrum of a step function is not concentrated at one wavenumber (Jenkins and Watts 1968)] and through their collective distribution in space (Saffman 1971).

The averaging period of 1 yr is not sufficient to precisely determine the area-averaged surface kinetic energy for the ICC sequence. Nevertheless, we see a trend of increasing energy with increasing resolution within the sampling uncertainty (Fig. 7). Furthermore, as a function of $k_{\text{max}} = \pi \Delta x^{-1} \rightarrow \infty$, an extrapolation of a velocity spectrum slope of -2 would imply a relatively slow asymptotic approach to energy convergence from below with a deficit of $O(k_{\text{max}}^{-1})$; this is not inconsistent with Fig. 7 within sampling uncertainty [cf. the more optimistic speculation about apparent energy convergence within the present ICC resolution range in Marchesiello et al. (2003)].

Tracer fields exhibit a somewhat different type of transition as resolution increases; ρ and T behave similarly near the surface but differ markedly in the subsurface. In the boundary layer the spectra for both tracers become shallower with increasing resolution toward a shape $\sim k^{-2}$. Also, spatial patterns for ρ (not shown) and T (Fig. 4d) are similar in their small scale features.³ Conversely, in the pycnocline the spectrum slope for T is between -2 and -3 , and for ρ it is around -3.5 . Qualitatively, we can understand this as being due to the surface intensification of the submesoscale transition and the strong dynamical constraints exerted in the surface boundary layer by the surface boundary condi-

² The high k spikes in the ICC0 T spectra indicate that the level of tracer dissipation implicitly provided by the tracer advection scheme in ROMS (Shchepetkin and McWilliams 1998) is close to its minimal acceptable value in this solution.

³ Note that the large-scale density gradient in the upper 40 m is strongly dominated by the temperature contribution (cf. T and S structures in Fig. 3), and this may be the main reason why limited compensation is observed in the mixed-layer ρ field.

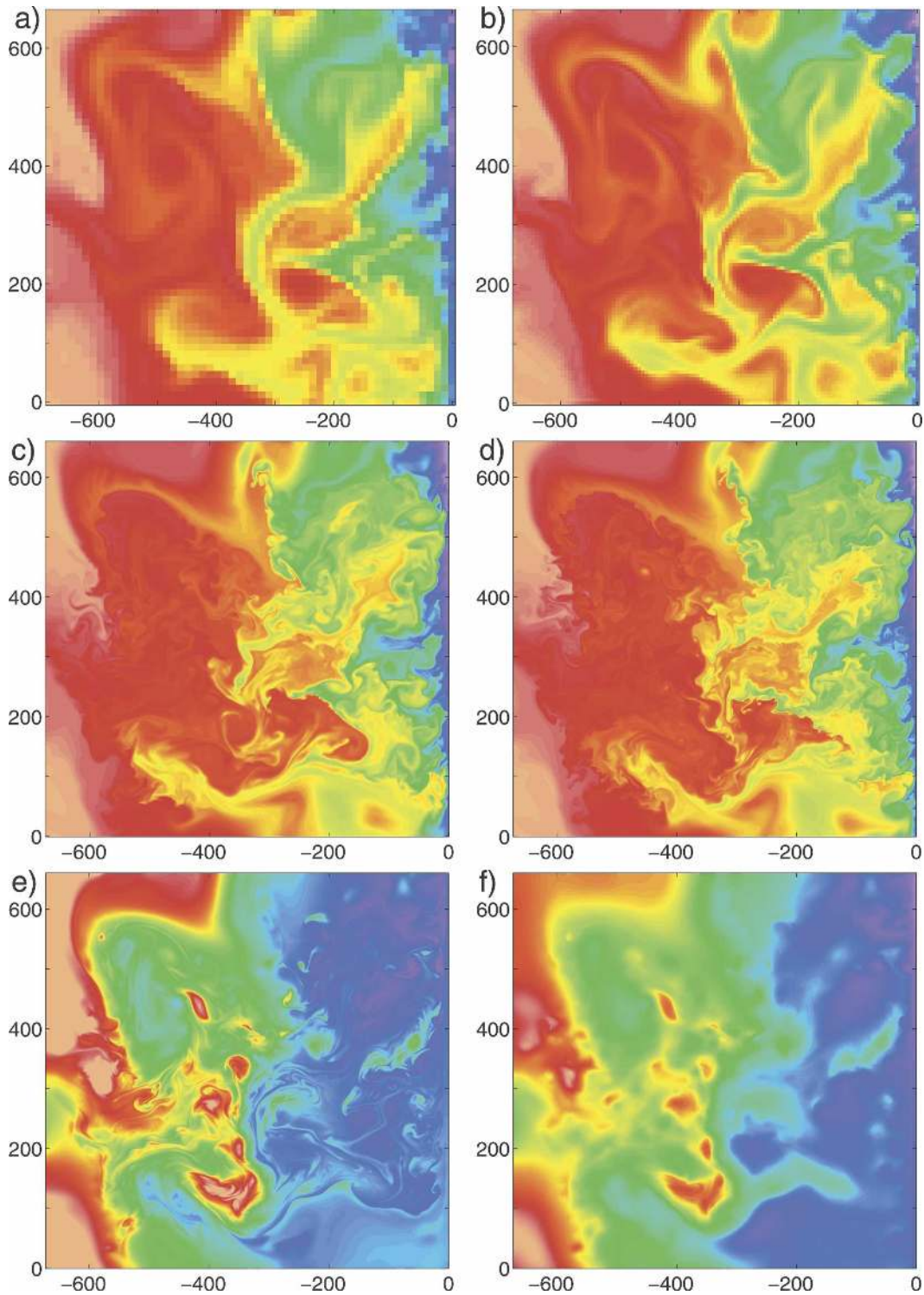


FIG. 4. Instantaneous $T(x, y)$ and $\rho(x, y)$ fields 30 days after ICC initialization: (a) T at 10-m depth in ICC12; (b) T at 10 m in ICC6; (c) T at 10 m in ICC1; (d) T at 10 m in ICC0; (e) T at 70 m in ICC0; (f) ρ at 70 m in ICC0. Temperature ranges are 10°–20°C at 10 m and 7.5°–16.5°C at 70 m, and the ρ range is 1024–1026.2 kg m⁻³.

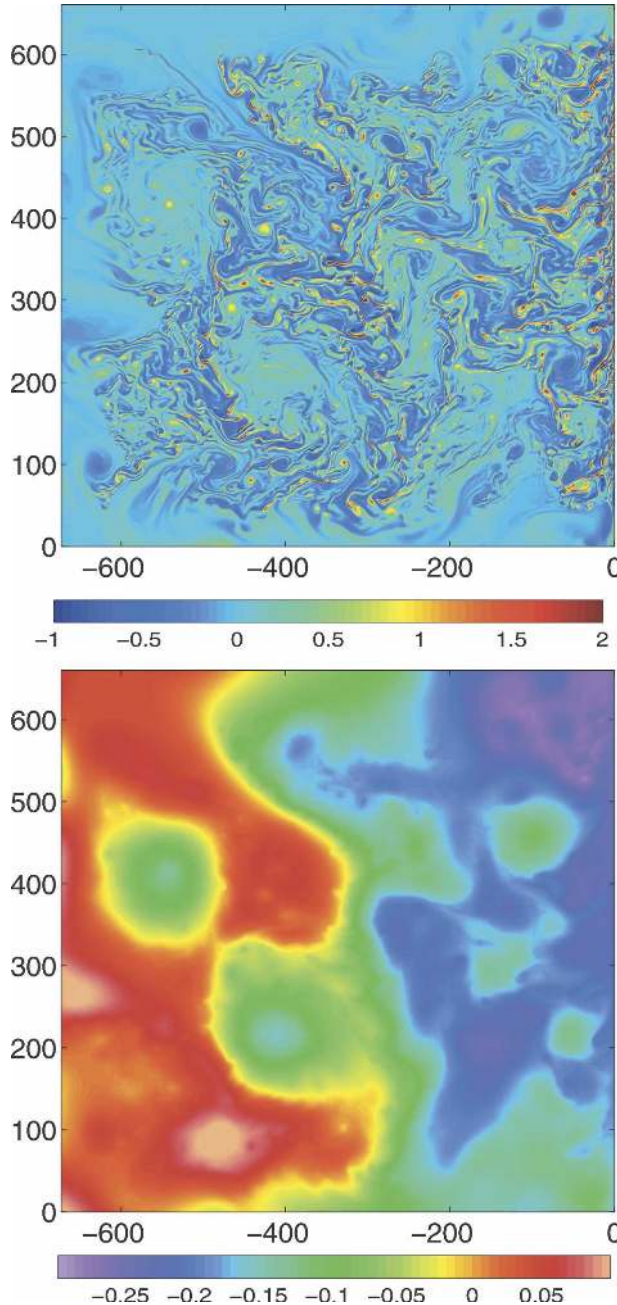


FIG. 5. (top) Surface vorticity $\zeta^z(x, y)$ (normalized by $f_0 = 8 \times 10^{-5} \text{ s}^{-1}$) and (bottom) sea level $\eta(x, y)$ at $t = 120$ days. Note the submesoscale filaments and vortices concentrated outside the mesoscale eddy cores and the dominance of cyclonic vorticity over anticyclonic.

tion $w \approx 0$ (conductive to frontogenesis and finescale tracer variance; Klein et al. 1998). In the pycnocline and below it the constraint of geostrophic balance is stronger, especially on ρ , since T has some finescale fluctuations that are density-compensated with S fluctuations. The relative degrees of finescale activity in T versus ρ

and in the surface versus the pycnocline are also evident in Fig. 4.

Thus, in the sequence of simulations from ICC12 to ICC0, a transition to vigorous submesoscale activity occurs. Based on the change in spectrum slopes with resolution, the transition seems essentially completed at the highest resolutions we have run (ICC1 and ICC0). Although further resolution increases would push the dissipation range—where the spectra steepen from their submesoscale-range slopes—toward even higher k , we do not expect significant further slope changes. This remark, however, overlooks any further regime changes that must somehow occur between submesoscale and microscale flows, but these are outside the resolutions achieved in this ICC sequence.

5. Intermittency and skewness

The spectra in Fig. 6 show that substantial variance for velocity and tracers resides in the submesoscale range. It is also true that much of the submesoscale structure is intermittently distributed in space and time, as suggested by the instantaneous patterns of T , ρ , and ζ^z in Figs. 4 and 5. A statistical manifestation of intermittency is a long-tailed probability density function (PDF) for tracer gradients, vorticity, and vertical velocity.

Density fronts are a primary source of intermittency, as indicated in the PDF for the horizontal density gradients $|\nabla_h \rho|$ (Fig. 8). There are long tails in the PDF near the surface, but they are not nearly as long in the pycnocline. The surface PDFs have approximately the functional form of an exponential distribution, as commonly seen in turbulence at high Reynolds numbers (Castaing et al. 1990). The total variance of the density gradient increases substantially with increased resolution (not shown), but after normalizing by the variance, the PDF tails increase only slightly with resolution. We interpret this as an indication that the front-generation process is implicit in the mesoscale eddy strain field in all our simulations, although the sharpness of the resulting fronts increases strongly into the submesoscale range when resolution allows it.

PDFs for ζ^z and w are shown in Fig. 9. They also show significant intermittency near the surface by long tails with approximately exponential shapes. But they also show significant asymmetry in the sign of the fluctuations: for ICC0 the skewness (i.e., normalized third moment of the PDF) for ζ^z at 10 m is +1.3, and for w at 20 m, it is -2.0 .⁴ The asymmetry of the vortex-

⁴ The normalized fourth related moment of the PDF, the kurtosis, is a measure for intermittency; for these two fields it has values, respectively, of 10 and 35, both of which are much larger than the Gaussian value of 3.

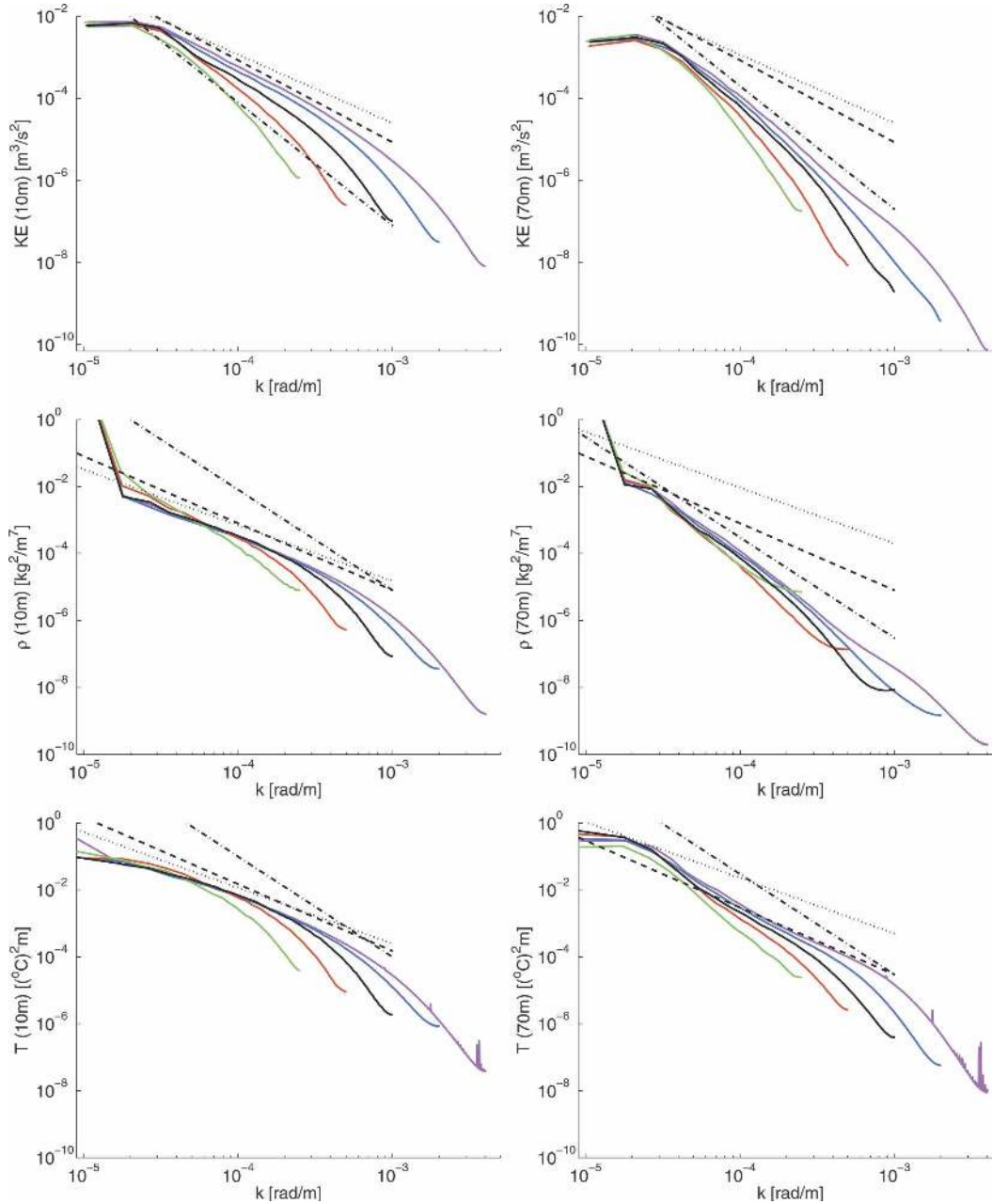


FIG. 6. Wavenumber spectra for (top) horizontal velocity (u , v), (middle) ρ , and (bottom) T at (left) 10- and (right) 70-m depth. Straight lines indicate $-5/3$ (dotted), -2 (dashed), and -3 (dot-dash) spectrum slopes. The five other lines correspond to the different cases whose wavenumber ranges increase from ICC12 to ICC0. Tracer spectra are time and cross-shore averages of individual 1D (alongshore) Fourier transforms, and velocity spectra are time and longitudinal-direction averages of 1D transforms of the average of both transverse velocity components [i.e., $u(y)$ and $v(x)$]. Sponge and nearshore regions have been excluded, and a Hanning window was applied to the fields prior to the Fourier transform.

stretching process favors cyclonic vorticity dominance for magnitudes larger than f , as does the limitation in anticyclonic $\zeta^z \geq -f$ due to centrifugal instability. These PDFs demonstrate that the types of asymmetry that develop in fronts—dominance of cyclonic vorticity and downward velocity near the surface (sec-

tion 2a of Part II)—are reflected in statistics for the fields as a whole. These asymmetries are essentially absent before the submesoscale transition (e.g., in ICC6) and in the pycnocline, and deeper after the transition (ICC0); they are also absent in quasigeostrophic dynamics.

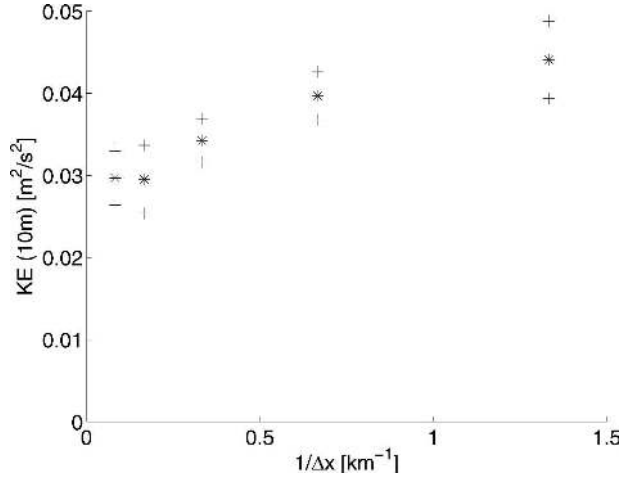


FIG. 7. Time- and area-averaged surface kinetic energy (asterisks) as a function of horizontal grid resolution, Δx^{-1} . Also plotted are the \pm rms fluctuation value (plus signs).

6. Flow decomposition

Our simulations exhibit a broad spectral range without an obvious break between mesoscale and submesoscale components (Fig. 6). To distinguish their relative contributions to different dynamical balances, we make a triple decomposition for all model variables V :

$$V = \bar{V} + \underbrace{(\tilde{V} - \bar{V})}_{V'} + \underbrace{(V - \tilde{V})}_{V''}. \quad (1)$$

This separates variables and flux contributions into mean (overbar), mesoscale (prime), and submesoscale (double prime) components based on appropriate filters, both very low pass (i.e., \bar{V}) and medium low pass (i.e., \tilde{V}). The very low pass filter is chosen as the (1 yr) time average. The choice of the medium low pass filter is more problematic because it requires defining a separation scale between mesoscale and submesoscale. In practice, we use a combination of temporal averaging over 2 days and horizontal smoothing (i.e., 2^n applications of a grid-scale, five-point operator with a 12-km smoothing length: $n = 4$ for ICC0, $n = 3$ for ICC1, $n = 2$ for ICC3, $n = 1$ for ICC6, and $n = 0$ for ICC12). Cross terms involving correlations between mesoscale and submesoscale quantities were checked and were found to be negligible in all cases.

Mean, mesoscale, and submesoscale root-mean-square (rms) velocity profiles are shown in Fig. 10 for two resolutions representative of mesoscale-resolving (ICC6) and submesoscale-resolving (ICC0) cases. The mean profiles are very similar. The additional eddy activity provided by increasing resolution preferentially goes to the submesoscale, especially for w . Indeed,

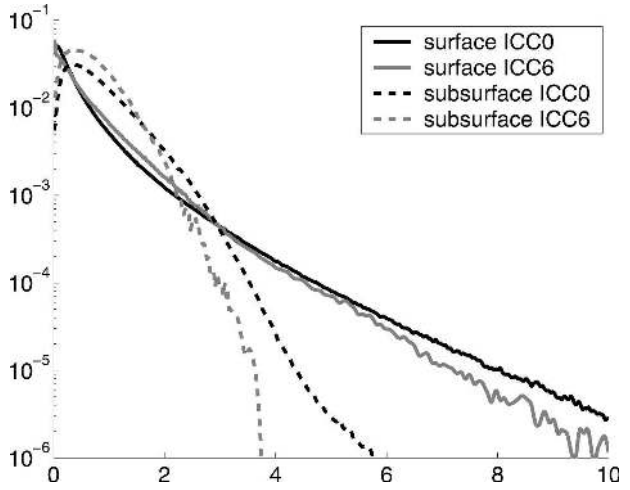


FIG. 8. Single-point PDFs for $|\nabla_h \rho|$ at 10- (solid lines) and 70-m depth (dashed lines) for ICC0 (black lines) and ICC6 (gray lines). They are calculated over the domain (excluding nearshore and sponge regions) and 100 independent times. Each curve is normalized so that both the total probability and the second moment (i.e., variance) are equal to 1.

w'_{RMS} does not significantly change between ICC6 and ICC0, whereas w''_{RMS} increases by a factor of 10. At a depth of 25 m, w''_{RMS} has a maximum of 12 m day $^{-1}$ and then sharply decreases with depth until it increases again in the pycnocline. Conditionally averaging w'' based on the local KPP boundary layer depth h shows the strong influence of h on w . The maximum of w''_{RMS} occurs at a depth of about $0.7h$. The changes in mesoscale and submesoscale (u, v) are modest compared to w , consistent with moderate mesoscale dominance of horizontal velocity and strong submesoscale dominance of vertical velocity.

7. Tracer fluxes and boundary layer restratification

Another important aspect of the transition occurs for the upper-ocean vertical eddy tracer fluxes. These increase in the submesoscale, relative to the mesoscale, and the w , T , and ρ fluctuations are correlated to act in favor of restratification within the boundary layer. The equilibrium, pointwise heat balance in ROMS is given by

$$\nabla_h \cdot \overline{\mathbf{u}_h T} + \partial_z \overline{w T} = \partial_z (\kappa \partial_z T), \quad (2)$$

with the subscript “ h ” denoting a horizontal vector, and the velocity and temperature fields triply decomposed as in (1). The effects of boundary fluxes and lateral diffusion are implicit in the transport divergence operators. In (2) the horizontal eddy heat flux plays a very important role, with cross-shore exchange balancing

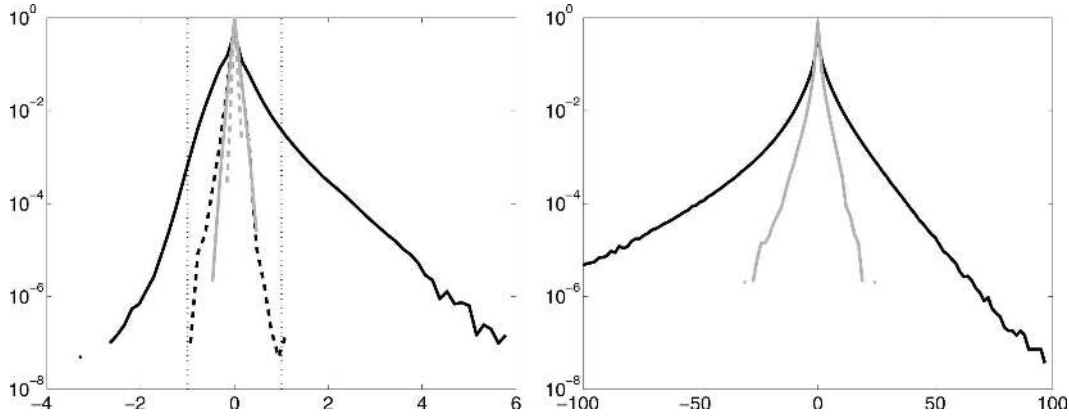


FIG. 9. Single-point PDFs for (left) ζ^z/f_0 at 10- (solid line) and 70-m depth (dashed line) and (right) w (day^{-1}) at 20-m depth for ICC0 (black lines) and ICC6 (gray lines). The dotted vertical lines in the left panel are $\zeta^z = \pm f_0$. These PDFs are normalized only so that the total probability is equal to 1.

offshore atmospheric warming and nearshore upwelling cooling (Marchesiello et al. 2003). The horizontal eddy flux is dominated by mesoscale eddies, and it changes only modestly across the ICC cases (not shown). However, the vertical eddy heat flux does exhibit a submesoscale transition. The flux divergences, $-\partial_z \overline{w''T''}$ and $-\partial_z \overline{w'T''}$, in Fig. 11 mainly act to restratify the boundary layer by warming above and cooling below. Note that this is a countergradient flux relative to the mean stratification (albeit only marginally so in the weakly stratified boundary layer). At the highest resolutions (ICC0 and ICC1), the submesoscale flux dominates over the mesoscale flux (which is largest in the nearshore upwelling zone); offshore there is a 10-fold increase of total eddy flux divergence magnitude from ICC12 to ICC0 (fivefold from ICC6 to ICC0). Expressed as an equivalent solar heat flux warming the upper half of the boundary layer, the contribution from

$-\partial_z \overline{w''T''}$ is equivalent to 80 W m^{-2} 200 km offshore and 300 W m^{-2} nearshore.

The heating rate by submesoscale vertical eddy flux divergence is about 5 times that by horizontal eddy flux. However, the consequences of $\overline{w''T''}$ for $\bar{T}(x)$ are limited. In going from 12- to 0.75-km grid spacing, there is only a 20% reduction in \bar{h} , an increase in stratification within the boundary layer (mostly near its base; even so it remains weak relative to the pycnocline), and little change in the surface temperature (SST)—less than 0.3°C in the domain average.

The explanation for the small sensitivity of $\bar{T}(x)$ to $\overline{w''T''}$ comes from the mean heat balance. We demonstrate this by comparing different terms in the domain-averaged balance between cases ICC6 and ICC0. Because the mean SST values for the two cases are close, the atmospheric heat fluxes are close (i.e., within 5 W m^{-2}), despite the SST-restoring formulation (section

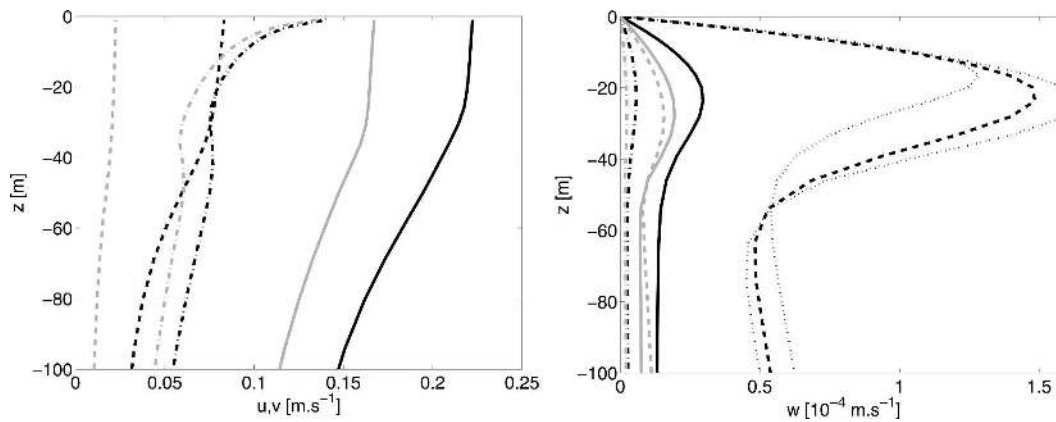


FIG. 10. Rms velocity profiles: mean (dot-dashed), mesoscale (continuous), and submesoscale (dashed). Each panel shows ICC0 (black lines) and ICC6 (gray lines). There are two additional w'' profiles for ICC0 (dotted lines), corresponding to conditional averages when the boundary layer is either between 20 and 30 m (with maximum rms w'' at 18 m) or between 30 and 40 m (with maximum rms w'' at 25 m).

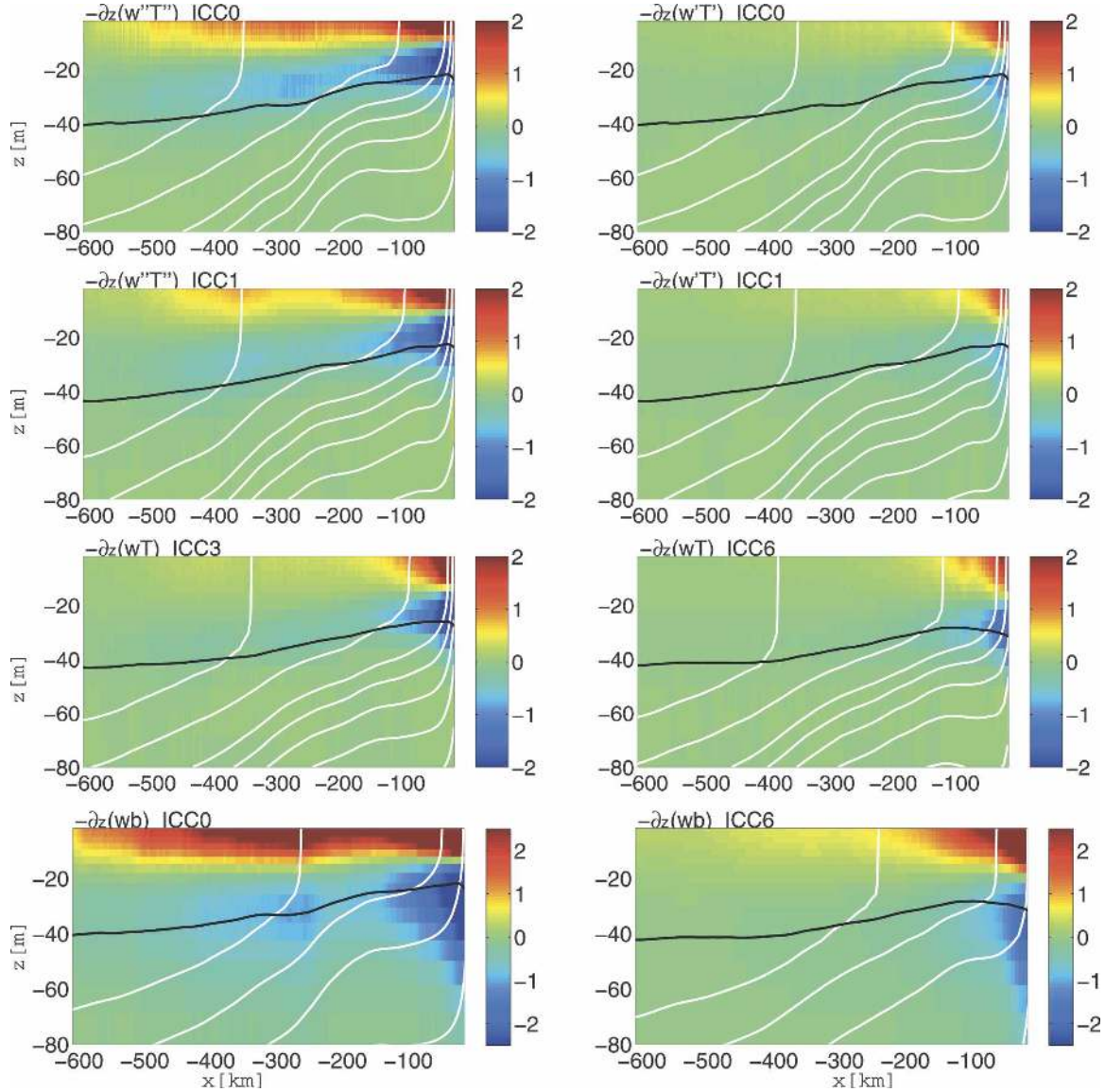


FIG. 11. Sections of time- and alongshore-averaged vertical eddy flux divergences for T ($10^{-6} \text{ }^{\circ}\text{C s}^{-1}$) and $b = -g\rho/\rho_o$ ($10^{-9} \text{ m}^2 \text{ s}^{-3}$) for different cases. For the heat flux panels, the white lines are mean isotherms $\bar{T}(x, z)$ (10° , 11° , 12° , 13° , 14° , 16° , and 18°C). For the buoyancy flux panels, the white lines are mean isopycnals $\bar{\rho}(x, z)$ ($24\text{--}25.5 \text{ kg m}^{-3}$ with 0.5 increments). The black line is boundary layer depth $\bar{h}(x)$.

2). Also, ICC6 and ICC0 have comparable mesoscale lateral heat fluxes since both cases adequately resolve the mesoscale dynamics. Therefore, the sum of the remaining terms in the local, upper-ocean heat balance (i.e., the submesoscale eddy flux, $-\partial_z \bar{w}''T''$ and the vertical mixing by boundary layer turbulence) does not change significantly between the two cases. This implies that

$$-\partial_z \bar{w}''T''|_{\text{ICC6}} + \partial_z \bar{w}''T''|_{\text{ICC0}} \approx -\partial_z \kappa \partial_z \bar{T}|_{\text{ICC6}} + \partial_z \kappa \partial_z \bar{T}|_{\text{ICC0}}, \quad (3)$$

where κ is the eddy diffusivity in the boundary layer from the KPP scheme. The two sides of this equation express the change in submesoscale flux (left) and vertical mixing (right) in the transition from 6- to 0.75-km grid spacing (Fig. 12). The eddy flux acts to restratify the upper ocean, and the mixing acts to destratify it. Both terms are substantially stronger after the submesoscale transition. The increase in the vertical heat flux with the submesoscale transition is balanced by an increase in vertical mixing. Since κ is large in most of the boundary layer because of wind-induced turbulent mix-

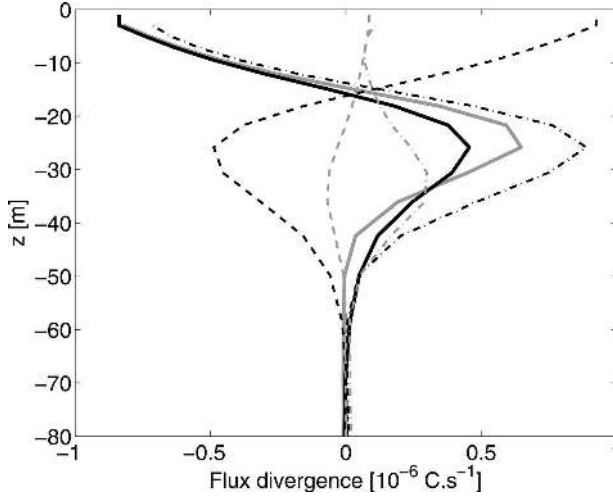


FIG. 12. Vertical profiles for terms in the mean heat balance. $-\partial_z w'' T''|_{ICC0}$ (black dashed line), $\partial_z \kappa \partial_z T|_{ICC0}$ (black dash-dotted line), $-\partial_z w'' T''|_{ICC6}$ (gray dashed line), and $\partial_z \kappa \partial_z T|_{ICC6}$ (gray dash-dotted line). Also shown are the transition changes (i.e., ICC6 – ICC0) in the left- and right-hand sides of (3): submesoscale eddy flux (black solid line) and vertical mixing (gray solid line).

ing (i.e., $\kappa \gtrsim 10^{-2} \text{ m}^2 \text{ s}^{-1}$ for $z > -h$), only a small change in $\partial_z T$ suffices to achieve balance. Therefore, the SST is little affected. The two sides of (3) are very similar, especially in the upper part of the boundary layer.

Although qualitatively similar, the submesoscale vertical eddy ρ (Fig. 11) and S fluxes (not shown) extend somewhat deeper than the boundary layer (i.e., also deeper than the T flux). So there is also a submesoscale transition in the vertical exchange between the boundary layer and pycnocline. We explain this as a consequence of the differences in the mean S and T distributions (Fig. 3), where the halocline is deeper than the thermocline.

8. Oceanic relevance

There is general agreement in magnitude between the simulated submesoscale activity in ICC0 and the available observations of fronts and vortices, including

some made in the California Current System. For example, the frontal and vortical features observed off Point Arena during the upwelling season in Flament et al. (1985) are visually very similar to the unstable regions in Fig. 4. Flament et al. (1985) estimate the strain rate near their unstable front as $8 \times 10^{-5} \text{ s}^{-1}$, which is a magnitude exceeded in about 20% of domain in ICC0. Paduan and Niiler (1990) measure a surface convergence on the cold side of an upwelling filament and relate it to the secondary circulation forced by the upwelling wind (see Part II for more details). They estimate a cold-side vertical heat flux of 400 W m^{-2} (i.e., equivalent to a temperature flux of $10^{-4} \text{ m}^\circ \text{C s}^{-1}$) in a 20-m-deep boundary layer; this is only modestly larger than the averaged values in Fig. 11. Table 1 compares our simulations with several other observational estimates made near strong submesoscale surface fronts. Such a comparison is ambiguous because of sampling differences that are very difficult to quantify.

Tracer and velocity spectra indicate the scale content of oceanic variability, albeit only as a rather gross measure. The only velocity spectrum estimate we know is a geostrophic one derived from sea surface slope (Stammer 1997). It captures only the upper-ocean geostrophic velocity contribution, and its meaningful wavelength range (100 km and above) barely overlaps the regime we are focusing on. In our simulations the geostrophic kinetic energy spectrum (i.e., for $g\nabla\zeta$) is fairly close to the total kinetic energy spectrum near the surface. For ICC0 and ICC1 the latter compare favorably with Stammer's generic results, namely, a kinetic energy spectrum peak around 400-km wavelength followed by a -2 power-law decay over the mesoscale range and extending into the submesoscale range up to a cutoff in the model's dissipation range. At wavelengths between 5 and 100 km, numerous measured tracer spectra provide robust evidence of a -2 roll-off in the upper ocean (Denman and Abbott 1988; Samelson and Paulson 1988; Ferrari and Rudnick 2000). The ICC0 and ICC1 spectra are consistent with this picture, again limited by the dissipation range where the spectra are steeper.

One of the most striking features in our solutions is

TABLE 1. Average of the 1% largest values of surface density gradient ($10^{-5} \text{ kg m}^{-4}$), vorticity (f units), and vertical velocity (m day^{-1}) for the simulations ICC12 and ICC0 (both 1-day average and instantaneous values), and for various submesoscale observational estimates near surface fronts: FAW85 (Flament et al. 1985), PN90 (Paduan and Niiler 1990), D91 (Dewey et al. 1991), and PR92 (Pollard and Regier 1992).

	ICC12	ICC0 (1 day)	ICC0 (instantaneous)	FAW85	PN90	D91	PR92
$ \nabla_h \rho $	2.3	6	12	3	—	12	5
ξ^z/f	$-0.11/+0.16$	$-0.4/+0.7$	$-0.6/+1.2$	—	$-0.3/+0.3$	$-0.4/+1$	$-0.3/+1.3$
w	$-2/+2$	$-30/+20$	$-65/+35$	10	$-15/—$	$-40/+40$	40

the ubiquity of tracer fronts, although some modulation of their intensity occurs because of the mesoscale. It is possible that our idealizations (primarily the constant upwelling favorable wind) lead to an overestimate of fronts frequency and intensity. However, high-resolution SST and ocean color imagery and their frontal-detection analyses (Ullman and Cornillon 2000; Miller 2004) suggest that submesoscale fronts are indeed ubiquitous in most oceanic regions, especially in regions of coastal upwelling, where temperature gradients are large and frontal detection is relatively easy (Castelao et al. 2006; Ullman et al. 2007).

9. Summary and discussion

By a computational experimental path that follows the changes in equilibrium dynamics for an idealized subtropical, eastern boundary, upwelling current system, we have demonstrated a regime transition that occurs for the submesoscale regime. The transition does not significantly alter the dominant mesoscale flow structures and their lateral material eddy fluxes, but it adds a new component to the flow with sharp near-surface density fronts and associated submesoscale instabilities and vortices. The submesoscale vertical velocity and vorticity magnitudes are much stronger than mesoscale ones. The emergent submesoscale currents are spawned and sustained from the mesoscale eddy field that has its own origin in the instability of the mean upwelling current system. The most important submesoscale eddy tracer flux provides a vertical restratification in the upper ocean that is countered by enhanced boundary layer vertical mixing. In this regard, the consequences of resolving submesoscale processes are modest for the mean fields, although they are significant for the associated mean tracer balances as well as for the kinetic energy balance (Part III), the associated tracer fluctuation spectra, and their dynamical balances.

The near cancellation between submesoscale restratification flux and boundary layer turbulent mixing may be overestimated by the posing of our simulations with steady forcing. In realistic conditions, upwelling-favorable and relaxation events will alternate on synoptic scales (from 1 to ~15 days). Every time the wind slackens and the boundary layer turbulence is reduced, we can expect the submesoscale to greatly speed up the upper-ocean restratification, thereby strongly affecting the mean tracer structure.

In more general terms, a subtropical eastern boundary current regime is somewhat unusual because it is highly stratified and near-surface concentrated in even

its mean fields. This confines the nonquasigeostrophic motions (inferred from the shallow spectrum slopes, but see also section 5 of Part II and section 4 of Part III) into a very thin near-surface layer and probably restricts their amplitude [cf. the increase of rms w with the boundary layer depth in Fig. 10 and also Fox-Kemper et al. (2008)]. If other current systems, such as western boundary currents or the Antarctic Circumpolar Current, undergo a similar type of submesoscale transition, the consequences are likely to be larger and extend over a larger fraction of the water column.

The submesoscale vertical eddy fluxes for a particular tracer will depend on the mean tracer distribution itself. Therefore, they may be even more significant for tracers other than T and ρ with stronger vertical gradients. In particular, the role played by the submesoscale in biogeochemical material exchange across the nutricline and boundary layer interface may be quite important.

Nevertheless, the present simulations are only for a particular situation, and as yet we cannot say how common it is for a submesoscale transition to occur in the ocean. Apart from the preceding caveat about the high degree of near-surface confinement, an upwelling current system seems more generic than unique in its mesoscale eddy behaviors; hence, it seems likely that its mesoscale-to-submesoscale transition should also be generic. A favorable but limited assessment of this expectation is made in section 8. The submesoscale characteristics of our simulations are qualitatively consistent with existing in situ measurements made near surface fronts as well as with wavenumber spectra for upper-ocean tracers. Recent analyses of numerical solutions for flows with a deeper vertical extension (Fox-Kemper et al. 2008; Klein et al. 2008) add further support to this view.

Acknowledgments. The authors greatly appreciate discussions with Lien Hua, Patrice Klein, Guillaume Lapeyre, and François Colas. This research was supported by ONR Grants N00014-04-1-0401 and N00014-05-10293 and NSF Grants OCE-0221177 and OCE-0550227. Many of the computations were made at the National Center for Supercomputing Applications.

REFERENCES

- Barnier, B., L. Siefried, and P. Marchesiello, 1995: Thermal forcing for a global ocean circulation model using a three-year climatology of ECMWF analyses. *J. Mar. Syst.*, **6**, 363–380.
- Bartello, P., 2000: Using low-resolution winds to deduce fine structure in tracers. *Atmos.–Ocean*, **38**, 303–320.

- Barth, J., 1994: Short wavelength instabilities on coastal jets and fronts. *J. Geophys. Res.*, **99**, 16 095–16 115.
- Boccaletti, G., R. Ferrari, and B. Fox-Kemper, 2007: Mixed layer instabilities and restratification. *J. Phys. Oceanogr.*, **37**, 2228–2250.
- Brink, K., and T. Cowles, 1991: The coastal transition zone program. *J. Geophys. Res.*, **96**, 14 637–14 647.
- Capet, X., J. C. McWilliams, M. J. Molemaker, and A. F. Shchepetkin, 2008: Mesoscale to submesoscale transition in the California Current System. Part II: Frontal processes. *J. Phys. Oceanogr.*, **38**, 44–64.
- Castaing, B., Y. Gagne, and E. Hopfinger, 1990: Velocity probability density functions of high Reynolds number turbulence. *Physica D*, **46**, 177–200.
- Castelao, R. M., T. P. Mavor, J. A. Barth, and L. C. Breaker, 2006: Sea surface temperature fronts in the California Current System from geostationary satellite observations. *J. Geophys. Res.*, **111**, C09026, doi:10.1029/2006JC003541.
- Charney, J., 1971: Geostrophic turbulence. *J. Atmos. Sci.*, **28**, 1087–1095.
- Da Silva, A., C. Young, and S. Levitus, 1994: *Algorithms and Procedures*. Vol. 1, *Atlas of Surface Marine Data 1994*, NOAA Atlas NESDIS 6, 74 pp.
- Denman, K., and M. Abbott, 1988: Time evolution of surface chlorophyll patterns from cross-spectrum analysis of satellite color images. *J. Geophys. Res.*, **93**, 6789–6798.
- Dewey, R. K., J. N. Moum, C. A. Paulson, D. R. Caldwell, and S. D. Pierce, 1991: Structure and dynamics of a coastal filament. *J. Geophys. Res.*, **96**, 14 885–14 907.
- DiGiacomo, P. M., and B. Holt, 2001: Satellite observations of small coastal ocean eddies in the Southern California Bight. *J. Geophys. Res.*, **106**, 22 521–22 544.
- Durski, S., and J. Allen, 2005: Finite-amplitude evolution of instabilities associated with the coastal upwelling front. *J. Phys. Oceanogr.*, **35**, 1606–1628.
- Ferrari, R., and D. Rudnick, 2000: Thermohaline variability in the upper ocean. *J. Geophys. Res.*, **105**, 16 857–16 883.
- Flament, P., L. Armi, and L. Washburn, 1985: The evolving structure of an upwelling filament. *J. Geophys. Res.*, **90**, 11 765–11 778.
- Fox-Kemper, B., R. Ferrari, and R. Hallberg, 2008: Parameterization of mixed layer eddies. Part I: Theory and diagnosis. *J. Phys. Oceanogr.*, in press.
- Hoskins, B. J., and F. P. Bretherton, 1972: Atmospheric frontogenesis models: Mathematical formulation and solution. *J. Atmos. Sci.*, **29**, 11–37.
- , and N. V. West, 1979: Baroclinic waves and frontogenesis. Part II: Uniform potential vorticity jet flows—Cold and warm fronts. *J. Atmos. Sci.*, **36**, 1663–1680.
- Jenkins, G. M., and D. G. Watts, 1968: *Spectral Analysis and Its Applications*. Holden-Day, 525 pp.
- Klein, P., A.-M. Tréguier, and B. Hua, 1998: Three-dimensional stirring of thermohaline fronts. *J. Mar. Res.*, **56**, 589–612.
- , B. Hua, G. Lapeyre, X. Capet, S. Le Gentil, and H. Sasaki, 2008: Upper-ocean turbulence from high-3D-resolution simulations. *J. Phys. Oceanogr.*, in press.
- Large, W., J. McWilliams, and S. Doney, 1994: Oceanic vertical mixing: A review and a model with a nonlocal boundary layer parameterization. *Rev. Geophys.*, **32**, 363–403.
- Mahadevan, A., and A. Tandon, 2006: An analysis of mechanisms for submesoscale vertical motion at ocean fronts. *Ocean Modell.*, **14**, 241–256.
- Marchesiello, P., J. C. McWilliams, and A. F. Shchepetkin, 2001: Open boundary conditions for long-term integration of regional oceanic models. *Ocean Modell.*, **3**, 1–20.
- , —, and —, 2003: Equilibrium structure and dynamics of the California Current System. *J. Phys. Oceanogr.*, **33**, 753–783.
- McCreary, J., Y. Fukamachi, and P. Kundu, 1991: A numerical investigation of jets and eddies near an eastern ocean boundary. *J. Geophys. Res.*, **96**, 2515–2534.
- McWilliams, J. C., 1985: Submesoscale, coherent vortices in the ocean. *Rev. Geophys.*, **23**, 165–182.
- , 2003: Diagnostic force balance and its limits. *Nonlinear Processes in Geophysical Fluid Dynamics: A Tribute to the Scientific Work of Pedro Ripa*, O. U. Velasco Fuentes, J. Sheinbaum, and J. Ochoa, Eds., Kluwer Academic, 287–304.
- , M. J. Molemaker, and I. Yavneh, 2001: From stirring to mixing of momentum: Cascades from balanced flows to dissipation in the oceanic interior. *From Stirring to Mixing in a Stratified Ocean: Proc. 'Aha Huliko'a Hawaiian Winter Workshop*, Honolulu, HI, University of Hawaii at Manoa, 59–66.
- Miller, P., 2004: Multi-spectral front maps for automatic detection of ocean colour features from SeaWiFS. *Int. J. Remote Sens.*, **25**, 1437–1442.
- Mitchum, G., and A. Clarke, 1986: The frictional nearshore response to forcing by synoptic scale winds. *J. Phys. Oceanogr.*, **16**, 934–946.
- Molemaker, M. J., J. C. McWilliams, and I. Yavneh, 2005: Baroclinic instability and loss of balance. *J. Phys. Oceanogr.*, **35**, 1505–1517.
- Müller, P., J. C. McWilliams, and M. J. Molemaker, 2005: Routes to dissipation in the ocean: The 2D/3D turbulence conundrum. *Marine Turbulence: Theories, Observations, and Models*, H. Z. Baumert, J. Simpson, and J. Sündermann, Eds., Cambridge University Press, 397–405.
- Paduan, J., and P. Niiler, 1990: A Lagrangian description of motion in northern California coastal transition filaments. *J. Geophys. Res.*, **95**, 18 095–18 109.
- Pedlosky, J., 1978: A nonlinear model of the onset of upwelling. *J. Phys. Oceanogr.*, **8**, 178–187.
- Pollard, R., and L. Regier, 1992: Vorticity and vertical circulation at an ocean front. *J. Phys. Oceanogr.*, **22**, 609–624.
- Rudnick, D. L., 1996: Intensive surveys of the Azores Front 2. Inferring the geostrophic and vertical velocity fields. *J. Geophys. Res.*, **101**, 16 291–16 304.
- Saffman, P., 1971: On the spectrum and decay of random two-dimensional vorticity distributions at large Reynolds number. *Stud. Appl. Math.*, **50**, 377–383.
- Samelson, R. M., and C. A. Paulson, 1988: Towed thermistor chain observations of fronts in the subtropical North Pacific. *J. Geophys. Res.*, **93**, 2237–2246.
- Shchepetkin, A. F., and J. C. McWilliams, 1998: Quasi-monotone advection schemes based on explicit locally adaptive dissipation. *Mon. Wea. Rev.*, **126**, 1541–1580.
- , and —, 2005: The Regional Oceanic Modeling System (ROMS): A split-explicit, free-surface, topography-following-coordinate ocean model. *Ocean Modell.*, **9**, 347–404.
- , and —, 2006: Computational kernel algorithms for fine-scale, multi-process, long-time oceanic simulations. *Handbook of Numerical Analysis: Special Volume: Computational Methods for the Atmosphere and the Oceans*, R. Temam and J. Tribbia, Eds., Elsevier, in press.

- Stammer, D., 1997: Global characteristics of ocean variability estimated from regional TOPEX/Poseidon altimeter measurements. *J. Phys. Oceanogr.*, **27**, 1743–1769.
- Thomas, L. N., 2005: Destruction of potential vorticity by winds. *J. Phys. Oceanogr.*, **35**, 2457–2466.
- , and C. M. Lee, 2005: Intensification of ocean fronts by down-front winds. *J. Phys. Oceanogr.*, **35**, 1086–1102.
- Ullman, D. S., and P. C. Cornillon, 2000: Evaluation of front detection methods for satellite-derived SST data using in situ observations. *J. Atmos. Oceanic Technol.*, **17**, 1667–1675.
- , —, and Z. Shan, 2007: On the characteristics of subtropical fronts in the North Atlantic. *J. Geophys. Res.*, **112**, C01010, doi:10.1029/2006JC003601.
- Voorhis, A., and J. Bruce, 1982: Small-scale surface stirring and frontogenesis in the subtropical convergence of the western North Atlantic. *Deep-Sea Res.*, **40** (Suppl.), 331–337.